

ARTICLE OPEN



Phase field modeling with large driving forces

Jin Zhang¹✉, Alexander F. Chadwick¹, David L. Chopp² and Peter W. Voorhees¹

There is growing interest in applying phase field methods as quantitative tools in materials discovery and development. However, large driving forces, common in many materials systems, lead to unstable phase field profiles, thus requiring fine spatial and temporal resolution. This demands more computational resources, limits the ability to simulate systems with a suitable size, and deteriorates the capability of quantitative prediction. Here, we develop a strategy to map the driving force to a constant perpendicular to the interface. Together with the third-order interpolation function, we find a stable phase field profile that is independent of the magnitude of the driving force. The power of this approach is illustrated using three models. We demonstrate that by using the driving force extension method, it is possible to employ a grid size orders of magnitude larger than traditional methods. This approach is general and should apply to many other phase field models.

npj Computational Materials (2023)9:166; <https://doi.org/10.1038/s41524-023-01118-0>

INTRODUCTION

The phase field method is a promising tool for materials design. For this to become a reality, it is essential to be able to employ realistic materials parameters in a phase field model. Despite the remarkable success of the phase field method in modeling microstructure evolution and computational design of materials, there are still barriers to achieving quantitative prediction for engineering problems. The phase field method employs a diffuse interface to obviate the need to track the interface but introduces an additional length scale of the diffuse interface thickness. A minimum number of grid points across the diffuse interface is needed to maintain accuracy and prevent pinning¹, which leads to the high computational cost of phase field simulations. One milestone in the development of quantitative phase field models is the introduction of methods that allow orders of magnitude larger interfacial widths than the physical interface width while still capturing the correct sharp interface behavior^{2,3}. Many recently developed phase field models follow this idea to employ a thicker interface width^{4–9}.

Large driving forces are common in engineering problems and phase field simulations. In the sharp-interface context, the driving force is related to an appropriate free energy jump at the interface that is responsible for the interface movement. The driving force is defined only at the interface. The magnitude of the driving force can be large for interface kinetic-limited growth like rapid solidification, electrodeposition, island growth on the surface, oxidation, and corrosion. In many other cases, the interface is assumed to be at local equilibrium, and the (sharp-interface) driving force has a small magnitude. In the diffuse-interface context, e.g., phase field models, the driving force is defined everywhere in the system; therefore, it can vary across the diffuse interface. In realization of the local equilibrium in a phase field model, the local equilibrium is valid to the first-order asymptotics⁷. Even if the physical driving force is small, higher-order asymptotic terms can still act as a large driving force, especially when the diffuse interface width is large. Therefore, in this context, a large driving force means a large apparent driving force: either due to a large physical/sharp-interface driving force or a large diffuse-interface driving force resulting from a large diffuse interface width.

These large *apparent* driving forces impose a strong upper bound on the interface width. This upper bound limits the spatial grid size to nanometers or even sub-nanometers, prohibiting the application of phase field models to practical system sizes ranging from micrometers to millimeters. The resulting computational cost is one of the most fundamental issues in quantitative phase field modeling. This limitation can be dramatic when considering stoichiometric line compounds, for example, where commonly employed parabolic free energies can be numerically unstable when trying to capture the correct composition¹⁰. Adaptive mesh refinement and advanced time integration methods may mitigate the problem, but they introduce additional numerical complexity. Various options are proposed to enable a larger grid size. Traditionally, the stability limit of the third-order interpolation is thought to be thermodynamic in nature. The most common strategy is using higher-order interpolations, like the widely used fifth-order interpolation¹¹, to make the free energy thermodynamically stable. Another is reformulating the evolution equations by a nonlinear transformation of the phase field function to a signed-distance type¹. A third strategy is the sharp phase field method^{12,13}, which employs a discrete free energy to resolve the interface with as little as one grid point. However, it is not easy to extend these methods to general numerical techniques with unstructured meshes, and it is not straightforward to apply them to some existing phase field models. A common feature of all previous strategies is that they rely on the surface energy term in the phase field equation to stabilize the traveling wave structure of the phase field profile; therefore, they do not fundamentally solve the stability problem, and the phase field profile will eventually break if the driving force is large enough. Recently, a stabilization method has been proposed where the surface energy is increased for the potential and the normal component of the Laplacian of the order parameter, while the physical surface energy is kept for the rest of the Laplacian¹⁴. This approach has addressed part of the large driving force issue, but it has not been extended to the most general cases with coupled fields or other phase field models. The last strategy is simply using unrealistic parameters in the model, but this precludes quantitative predictions, comparison with experiments, and models that can be used for materials design.

¹Department of Materials Science and Engineering, Northwestern University, Evanston, IL 60208, USA. ²Department of Engineering Sciences and Applied Mathematics, Northwestern University, Evanston, IL 60208, USA. ✉email: jzhang@northwestern.edu

We propose a strategy to maintain an unconditionally stable phase field profile independent of the magnitude of the driving forces. We find that the stability issue is caused by a nonlinear variation of the driving force within the diffuse interface instead of the magnitude of the driving force. By noticing that the traveling wave structure can be maintained without the surface energy term using the third-order interpolation and a constant driving force, we propose a driving force extension method to project the driving force to a constant perpendicular to the interface. The limitation on grid size by the driving force is eased, making it possible to freely choose grid size orders of magnitude larger than previous methods. We demonstrate the versatility of our method with several applications: a single order parameter case and two general cases with coupling fields. The proposed method correctly captures the Gibbs-Thomson effect and is straightforward to be applied to higher dimensions. The proposed driving force extension method only needs a simple modification of the phase field equation; therefore, it is straightforward to apply to existing phase field models and easy to adapt to many numerical techniques. Our vision is that this method could be employed in most existing phase field models to handle the stability problem due to large *apparent* driving forces, thereby initiating a significant step forward in using the phase field method as a quantitative tool in materials design.

We first explain the stability issue due to large driving forces and propose the driving force extension method. We demonstrate the proposed strategy using a driven Allen-Cahn equation employed as a model for additive manufacturing^{15,16} and compare it with traditional methods. Once validated, the method is applied to a more general problem with coupled fields: a solidification problem with coupling between a phase field and a concentration field. We use both the Kim-Kim-Suzuki (KKS) model¹⁷ and the grand potential model⁶ to demonstrate its generality. We further validate the driving force extension method's ability to capture the capillary effect and perform calculations in higher dimensions.

RESULTS

Driving force extension method

The phase field method uses one or more order parameters u to describe interfaces in materials. The order parameter has constant values in bulk phases and has a sharp transition at the interface. The evolution equation of a nonconserved order parameter u in a phase field model has the following general form

$$\tau \frac{\partial u}{\partial t} = \kappa \nabla^2 u - mg'(u) + p'(u)F, \quad (1)$$

where τ is a time scale determined by the kinetics of the interface, $g(u)$ is a double-well function for a single order parameter, and a multi-well function for multiple order parameters, $p(u)$ is an interpolation function, $\kappa = 6\gamma/l$ and $m = 3\gamma/l$ for $g(u) = u^2(1-u)^2$ are model parameters related to the surface energy γ and the diffuse interface width l , and F is the driving force, which can be a function of relevant field variables, *e.g.*, temperature, concentration, mechanical displacement, and electrostatic potential. Phase field models with a different form than Eq. (1), like the hyperbolic phase field model¹⁸, are not considered in this work. Generally, F is a function of space and time. The driving force F typically varies across the diffuse interface, as shown in Fig. 1b (see the "Methods" section for the specific form of F used to construct Fig. 1). Here we define the apparent driving force F_{app} as the maximum of the absolute value of F within the diffuse interface: $F_{\text{app}} = \max\{|F(\mathbf{x})| : u(\mathbf{x}) > \varepsilon \cup u(\mathbf{x}) < 1 - \varepsilon\}$ for a small positive number $\varepsilon \ll 1$. A large apparent driving force can result from either a large physical driving force or a large diffuse interface width. Frequently seen in phase field simulations, especially with a large F_{app} , the phase field profile becomes unstable, as shown by the dashed line

in Fig. 1a. This deviates considerably from the desired traveling wave structure of the phase field profile, as shown by the solid line in Fig. 1a. To better understand the problem, let us rearrange Eq. (1) by substituting the expressions of κ and m :

$$\tau \frac{\partial u}{\partial t} = \frac{6\gamma}{l} \left(l^2 \nabla^2 u - \frac{1}{2} g'(u) \right) + p'(u)F. \quad (2)$$

The first term on the right-hand side is a surface energy term, stabilizing the phase field profile and maintaining its traveling wave structure during evolution. The second term is a driving force term, which typically breaks the traveling wave structure. Since the surface energy part scales with the inverse of the diffuse interface width l , when the driving force F is large, a small interface width, and consequently a small grid size, is necessary to balance the surface energy and the driving force terms. For example, the driving force corresponding to a typical overpotential $\eta = 0.1$ V in electrochemical systems is on the order of $F \sim \mathcal{F}\eta/V_m \approx 10^9 \text{ Jm}^{-3}$, where \mathcal{F} is the Faraday constant and V_m is the molar volume. For a typical surface energy of $\gamma = 0.2 \text{ Jm}^{-2}$, the interface width to balance the two terms is $l \approx 1$ nm. The grid size will be even smaller to properly resolve the diffuse interface since typically six to eight grid points across the interface are needed. Here, we define a large driving force as the case when $F_{\text{app}} \gg 6\gamma/l^{11,14}$.

Here, we explore a different way to stabilize the phase field profile. To solve this problem of an unstable phase field profile under a large driving force, we start with two observations. First, in the sharp limit ($l \rightarrow 0$), the driving force is only defined at the interface. Second, if F is a constant perpendicular to the interface, the traveling wave solution is stable even without the surface energy term. This can be seen by substituting the third-order interpolation function $p(u) = u^2(3-2u)$ and the steady-state phase field profile $u = \frac{1}{2}(1 - \tanh \frac{x-vt}{2l})$ into Eq. (2) and neglecting the surface energy term

$$-v\tau \frac{\partial u}{\partial x'} = -6lF \frac{\partial u}{\partial x'}, \quad (3)$$

where $x' = x - vt$ is a moving coordinate with velocity v relative to the fixed coordinate x . Intuitively, a constant F keeps the traveling wave structure; otherwise, v will vary across the diffuse interface, leading to an unstable profile. Mathematically, as will be shown in the "Discussion" section and Supplementary Note, any F that can be written as a constant plus an anti-symmetric function preserves the traveling wave structure. This analysis also works for other phase field profiles, like the one related to the double-obstacle potential. See Supplementary Note for details.

In many practical applications, F is coupled, *e.g.*, to the temperature or the concentration field, which can be nonlinear across the diffuse interface. To address the stability problem with a nonlinear driving force, we propose the following projection of the driving force to a constant perpendicular to the interface

$$\mathcal{P}(F(\mathbf{x}, t)) = F(\mathbf{x}_\Gamma, t), \quad (4)$$

where $\mathbf{x}_\Gamma(\mathbf{x}) = \{\mathbf{y} : \min_{\mathbf{y} \in \Gamma} |\mathbf{y} - \mathbf{x}|\}$ is the closest point to \mathbf{x} on the interface Γ . See Fig. 1b for an example in 1D and Fig. 1c-d for 2D. The interface can be regarded as the contour $u = 1/2$. It can be shown that the projected driving force is constant perpendicular to the interface $\nabla \mathcal{P}(F(\mathbf{x})) \cdot \nabla u = 0^{19}$, which can also be seen in Fig. 1d. With this projection of the driving force, we introduce a simple modification of the evolution equation (Eq. (1))

$$\tau \frac{\partial u}{\partial t} = \kappa \nabla^2 u - mg'(u) + p'(u)\mathcal{P}(F). \quad (5)$$

This projection \mathcal{P} can be made with efficient velocity extension algorithms for higher dimensions and general spatial discretizations^{19,20}. See the "Methods" section for a summary.

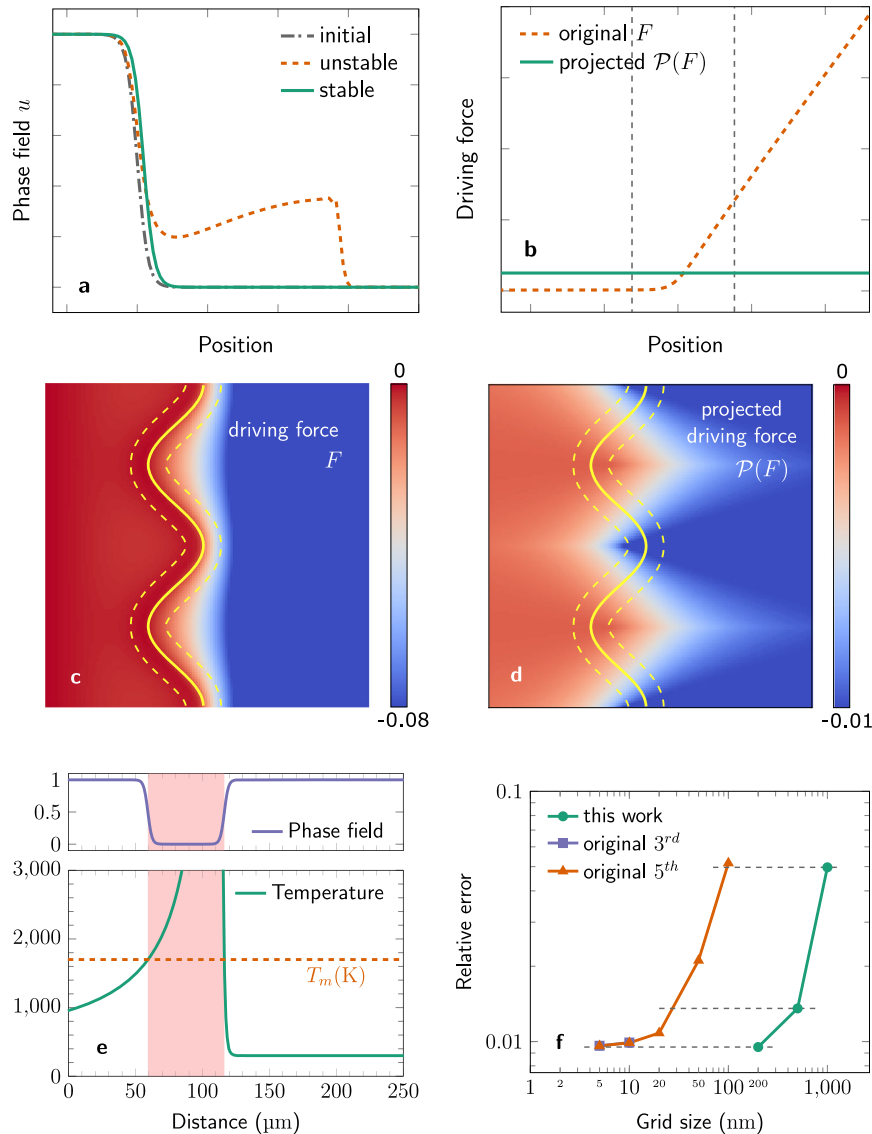


Fig. 1 Stability issue of the phase field profile and the driving force extension method. **a** A schematic example of an unstable phase field profile (dashed line) for a traveling wave starting from the dot-dashed line. A similar traveling wave with the proposed method is stable (solid line) at the same time. **b** An example of the proposed driving force extension method projects the original driving force (thick dashed line) to a constant (solid line). The two vertical dashed lines mark the diffuse interface between $u = 0.01$ and $u = 0.99$. **c** An example of the original driving force in 2D, where the solid line marks the location of the interface and the dashed lines mark the diffuse interface between $u = 0.01$ and $u = 0.99$. A cutoff at -0.08 is used to better visualize the driving force variation within the diffuse interface. **d** An example of the projected driving force in 2D. **e** The phase field variable and the temperature profile generated by a point laser source moving to the right at a constant speed. The shaded region shows the melting pool. **f** The relative error of the interface velocity as a function of grid size for the proposed method and the original method with the third- and fifth-order interpolations. The dashed lines provide a guide of the same relative error.

Application 1: additive manufacturing

We start from the simplest case: a driven Allen-Cahn equation with a nonlinear driving force (due to the nonlinear temperature field). Figure 1e shows the modeling problem. A moving laser source generates a temperature field (Eq. (10)). The liquid phase exists in regions above the melting temperature T_m , and the solid presents in regions below. The phase field variable equals zero/one in the bulk liquid/solid. Details of the form of the driving force, the phase field model, materials parameters, and initial and boundary conditions are provided in the “Methods” section. The system has two interfaces, one solid-liquid interface and one liquid-solid interface, as shown in Fig. 1e (the shaded region marks the liquid domain). The evolution of their location is simulated by the proposed driving force extension

method and compared with results by traditional methods with both third- and fifth-order interpolation functions. The relative errors of the interface velocity are compared with the analytical solution and shown in Fig. 1f. The traditional method with the third-order interpolation is the least stable and breaks above 10 nm grid size. The fifth-order interpolation has a similar order of accuracy to the third-order interpolation but is much more stable: it is stable up to a grid size of 100 nm. The proposed method is stable with a 1 μm grid size. As shown in Fig. 1f, the driving force extension method has a similar convergence behavior as the traditional method, but with a grid size more than one order of magnitude larger than the state-of-art methods with similar accuracy (see gray dashed lines in Fig. 1f), making a significant reduction in computational cost.

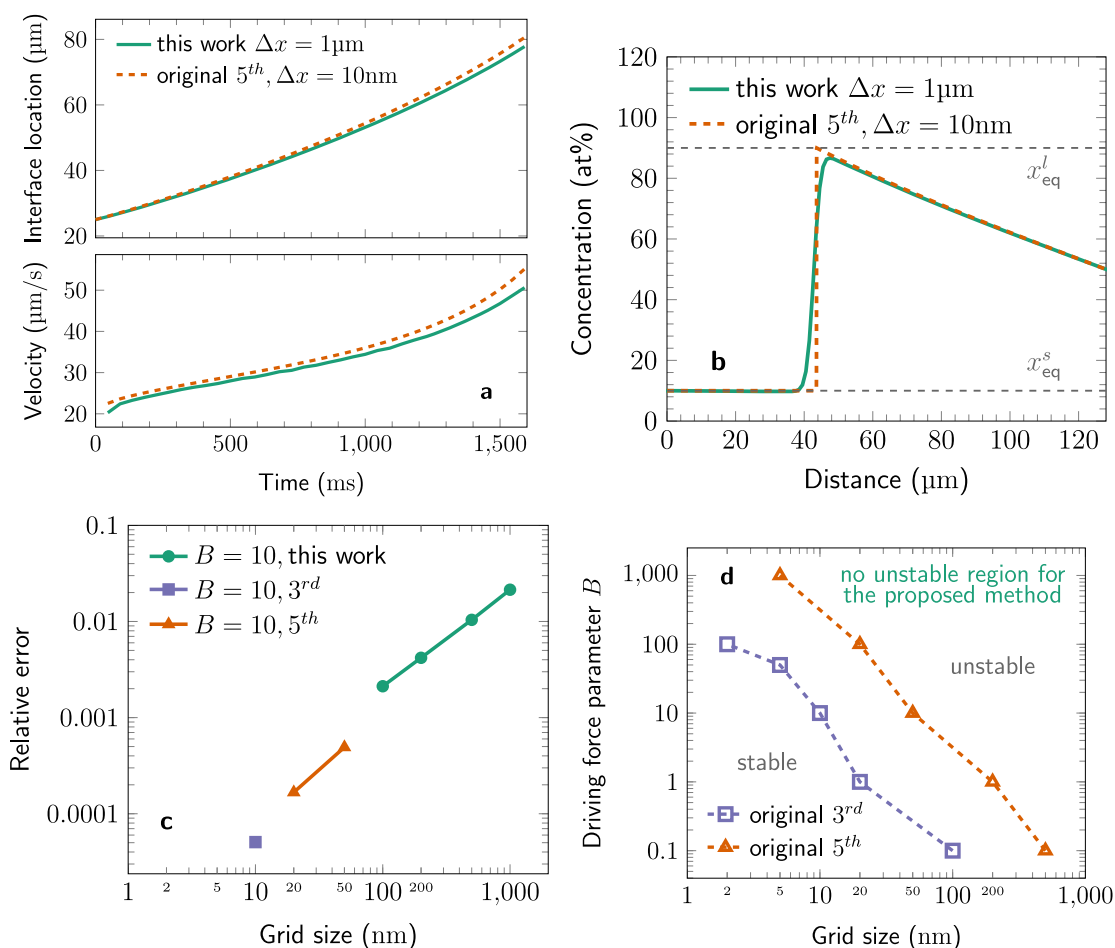


Fig. 2 Solidification. **a** Evolution of the interface location and velocity. The proposed method uses a grid size 100 times larger than the original method with fifth-order interpolation. **b** The concentration profile for the proposed method with a grid size of 1 μm and the original method with a grid size of 10 nm. Local equilibrium concentrations x_{eq}^l and x_{eq}^s at the interface are recovered. **c** Relative error of the interface location as a function of grid size for various methods. The driving force parameter B controls the magnitude of the driving force and is dimensionless by an energy scale $RT/V_m = 2.25 \times 10^8 \text{ J m}^{-3}$. **d** Upper limit of the driving force for a given grid size for the original method with third- and fifth-order interpolations. The proposed method has no unstable region.

Application 2: solidification

The previous application uses a single order parameter. Here we apply our method to a more general case where the order parameter is coupled with a concentration field. The order parameter describes phase transformation, and the concentration describes solute diffusion. In this test case, constant undercooling is applied during the solidification of a binary alloy, and the growth is assumed to be diffusion-limited and the concentrations at the interface are given by the local equilibrium condition ($L = L_{\text{eq}}$). The evolution of the interface and concentration are coupled and modeled by the KKS model. Details on the model, materials parameters, and initial and boundary conditions are provided in the “Methods” section. Although the driving force is expected to be small with the local equilibrium condition (it is zero in the sharp interface limit for a planar interface), the interface can still be unstable up to a finite value of the driving force (due to a diffuse interface), as shown in Fig. 2d. Figure 2a compares the evolution of the interface location and velocity determined by traditional and proposed methods for a driving force parameter $B = 10$ (curvature of the parabolic free energy; see Eq. (15) for the definition; made dimensionless by RT/V_m). In real systems, B can be large, especially for systems with compounds¹⁰. A comparison of the concentration profile is shown in Fig. 2b. It can be seen that

even with a grid size 100 times larger, the proposed method can correctly capture the bulk concentration and local equilibrium interfacial concentrations and gives a reasonable prediction of the interface location and velocity (the relative error in the velocity is typically about 5% in Fig. 2a). Since there is no analytical solution, the simulation result of the fifth-order interpolation function with a 10 nm grid size is used as a reference for the relative error. Figure 2c shows the relative error of interface location as a function of the grid size for $B = 10$ (see Supplementary Note for numerical details). For this case, the third- and fifth-order interpolations are stable up to a grid size of 10 nm and 50 nm, respectively. The proposed method is stable with a grid size of 1 μm (system size is 128 μm). Unlike the previous single order parameter case, there is an intrinsic modeling error related to the interface width in the KKS model, as the model is based on thin interface asymptotics. As seen in Fig. 2c, the error is virtually proportional to the interface width, independent of the methods used. The driving force extension method has small effect on the convergence rates. Denoting the error as h^p , where h is the grid size, we have $p = 1.18$ for the traditional method (fifth-order interpolation) and $p = 1.00$ for the proposed method. Generally, for the same grid size, the driving force extension method tends to have a slightly larger error (1.5 to 2 times) than the original method, due to discretization and interpolation errors in the

numerical implementation. For example, with $B = 1$ the relative error for the fifth-order interpolation with a grid size of 100 nm is 1.44×10^{-3} while with the proposed method, the relative error is 2.12×10^{-3} for the same grid size and timestep size. However, our method enables a larger grid size where traditional methods are unstable. A larger value of B means larger driving forces. As shown in Fig. 2d, there is an upper limit on how large the driving force can be resolved properly by the traditional methods with a given grid size: the larger the driving force, the smaller the maximum grid size that can be used. For $B = 1000$, the traditional method with the fifth-order interpolation is only stable up to a grid size of 5 nm, while the proposed method is stable with a grid size of 1 μm . The proposed method not only reduces the number of grid points by a factor of 200, but also reduces the number of timesteps by a factor of 40000 for the same physical time, leading to a combined reduction of 8×10^6 . The proposed method erases the upper bound and is stable for any value of the driving force, significantly improving the computational efficiency.

Effect on capillarity

Another question is if the driving force projection in Eq. (5) affects the curvature dependant interfacial compositions, i.e., the Gibbs-Thomson effect. To investigate this question, we model a small circular particle embedded in a liquid and determine the interfacial concentration in the liquid (the matrix phase). The grand potential model is solved in polar coordinates with a quasi-steady-state assumption. The interfacial liquid concentration is measured by interpolation to the interface ($u = 0.5$) and compared with the one determined by the Gibbs-Thomson equation. The phase field model and materials parameters can be found in the

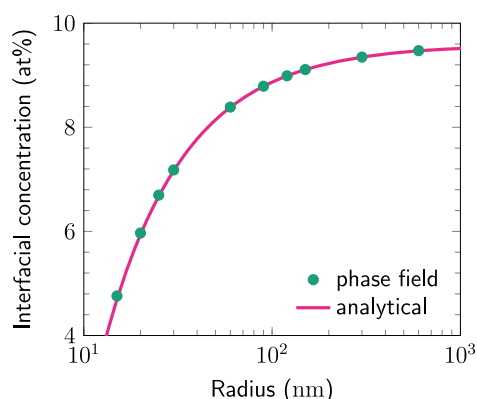


Fig. 3 The Gibbs-Thomson effect. The interfacial liquid concentration as a function of the particle size.

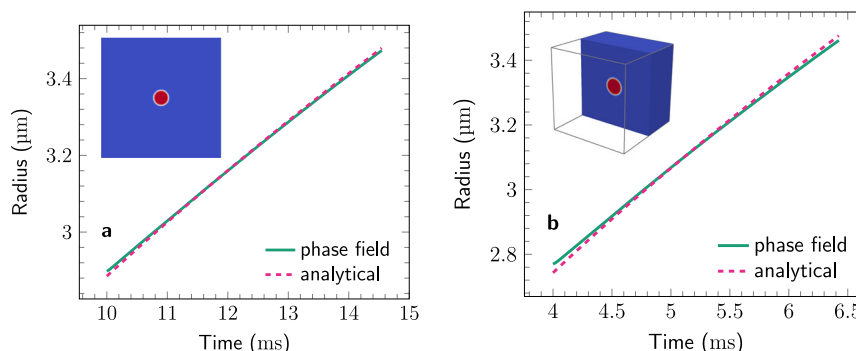


Fig. 4 Growing particle in a supersaturated liquid. Evolution of the particle radius of the proposed method compared with analytical solutions for 2D (a) and 3D (b), respectively. The insert shows the phase field.

“Methods” section. We choose a small particle size here to highlight the capillary effect. The simulated interfacial liquid concentration as a function of the particle radius is compared with the analytical solution in Fig. 3. This verifies that the proposed method captures the correct Gibbs-Thomson effect.

Application in 2D and 3D

Here we apply the proposed method in 2D and 3D. We model the evolution of a growing circular particle in a supersaturated solution using the KKS model (in the diffusion-limited regime). To minimize the effects of the domain boundary, the domain size is 51.2 μm in 2D and 32.0 μm in 3D. For $B = 1$, the evolution of the particle radius is compared with the analytical solution²¹ in Fig. 4a for 2D and in Fig. 4b for 3D, where a good match with the analytical solution is seen. The proposed method uses a grid size of 100 nm. In comparison, the traditional method with the fifth-order interpolation is *unstable* for the same grid size (Supplementary Fig. 1). For the 2D case, a detailed comparison between the proposed method and the traditional method for $B = 20$ is given in Table 1. The traditional method with the fifth-order interpolation is stable only with a grid size of 25 nm. Although with a slightly larger error (2.9 times), the proposed method is stable with a grid size four times larger (100 nm) and a timestep 16 times larger. Note the proposed method is still stable with $B = 1000$ and a grid size of 100 nm, while the traditional method is not stable with $B = 50$ and a grid size of 25 nm. For larger B in 2D or in 3D, comparison with the traditional method demands a significant amount of computational resources, and the behavior is expected to be similar to the 1D and 2D (small B) cases; therefore, fine-resolution simulations are not performed. Considering system size n (total number of grid points), the computational complexity of the extension is $\mathcal{O}(m \log m)$, where $m = n$ for the full grid and $m \sim n^{(d-1)/d}$ for a narrow band algorithm. The computational complexity of the stencil calculations is $\mathcal{O}(n)$. This is seen in Supplementary Fig. 2, that the relative cost of the extension versus the stencil calculation gets lower with increasing system size for both 2D and 3D. An increase in grid size enables not only a smaller system size, but also a smaller number of timesteps. Generally, if the grid size is increased by N times in d dimensions, the computational demand can be reduced by N^{2+d} times, with N^2 in the number of timesteps and N^d in the number of grid points. The theoretical speedup for the case given in Table 1 is $4^4 = 256$ while the actual computational time saved is a factor of 309. This super speedup may result from better utilization of memory and cache for the smaller system size. For a fixed system size, the computational time per timestep and grid of the driving force extension is similar to the stencil calculations, as shown in Supplementary Fig. 2. However, the benefit of a much smaller

Table 1. Results for the 2D case (KKS model with $B = 20$).

Methods	Grid size nm	Timestep ns	System size	Number of timesteps	stable?	Relative error	Time seconds
Traditional	25	28.41	2048 ²	160,000	yes	0.0883%	102938
Traditional	50	113.64	1024 ²	40,000	no	–	4879
Traditional	100	454.55	512 ²	10,000	no	–	310
This work	100	454.55	512 ²	10,000	yes	0.2521%	333

For the traditional method, the fifth-order interpolation is used. The relative error is the root-mean-square error of the radius compared to the analytical solution. The computational time (last column) is taken on one node (quest 11) of the Quest supercomputer (64-core Intel Xeon Gold 6338 CPU @ 2.0GHz, 256 GB DDR4 2666 MHz).

number of timesteps and grids is far beyond the overhead caused by the driving force extension.

DISCUSSION

Driving force profile across the diffuse interface

The stability issue is caused by a nonlinear variation of the driving force profile within the diffuse interface. We show that a constant driving force perpendicular to the interface can keep the traveling wave structure. This requirement can be relaxed to a driving force of an anti-symmetric form: a constant plus an anti-symmetric function with respect to the interface location $F(x) = F_0 + \sum_{i=1}^{\infty} a_i x^{2i-1}$, where $x=0$ is the interface. For any driving force with this anti-symmetric form, the traveling wave solution exists (see Supplementary Note). In principle, mapping the driving force to any function with this anti-symmetric form can solve the stability issue. However, mapping to a constant is the most straightforward from an implementation point of view.

Hitting the wall

For extremely large driving forces, the evolution equation can be approximated as

$$\tau \frac{\partial u}{\partial t} = p'(u)F = 6u(1-u)F. \quad (6)$$

When solving the equation with a computer, there is a truncation error due to machine precision (typically on the order of 10^{-16} for double precision). For the grid points with a value of u below the machine precision, u cannot be properly resolved numerically, resulting in zero $\partial u / \partial t$ even if the interface is already moving close to where the initial u is smaller than the truncation error. During evolution, the phase field profile seems to stop evolving or hit a wall. To solve this problem, we introduce neighboring information to approximate $p'(u)$ for those wavefront points (whose u is below machine precision but with at least one neighbor's u above) as

$$p'(u) = 6u(1-u) \approx -6\hat{n} \cdot \nabla u = 6|\nabla u|, \quad (7)$$

where \hat{n} is the unit normal vector of the interface. This introduces the effect from neighbors to bring the value of u above the machine precision. Note that this wavefront regularization is only needed for a few points; therefore, it does not introduce a considerable computational overhead. Moreover, if the driving force is not extremely large, the surface energy term can alleviate this problem and the wavefront regularization is unnecessary.

Curvature correction for higher dimensions

For 2D or 3D problems, we can correct the Laplacian operator based on the local curvature to better resolve the interface

kinetics. In practice, we replace $\nabla^2 u$ in Eq. (5) by

$$\nabla_c^2 u = \nabla^2 u - (\mathcal{P}(2\mathcal{H}) - 2\mathcal{H}) \frac{u(1-u)}{l}, \quad (8)$$

where $\mathcal{H} = \frac{1}{2} \nabla^2 \phi$ is the mean curvature, and ϕ is the signed distance function, which is a direct output from the driving force extension (see Eq. (20) in the “Methods” section for details). Considering the extra computational costs, we find that this correction is generally not favored compared to refining the mesh, but can be useful for cases that demand higher accuracy.

Numerical considerations

The proposed driving force extension method involves a simple modification of the phase field equation, as given in Eq. (5). It relies on the well-developed velocity extension algorithm¹⁹, which has already been implemented with efficient algorithms^{19,22,23} and has been parallelized and accelerated (e.g., on GPUs)^{23,24}. These algorithms can be directly applied to the proposed method.

In the current work, for the sake of simplicity, we solve all the equations with a forward-Euler time stepper and finite difference spatial discretization. However, the proposed method can be applied to other time integration schemes: multi-stage time stepping like the Runge-Kutta method, adaptive time stepping like the embedded Runge-Kutta method, and implicit time stepping like the backward differentiation formula (BDF), to name a few. Regarding spatial discretization, it is straightforward to incorporate the proposed method with other techniques like the pseudo-spectral method, the finite volume method, and the finite element method. Moreover, the velocity extension algorithm can work on unstructured meshes²⁵ and with adaptive mesh refinement²⁶, so the proposed method can cooperate with various mesh techniques.

The numerical implementation of the velocity extension algorithm employed in this work uses a cubic interpolation and a first-order upwind scheme. The accuracy of the velocity extension can be improved by using a higher-order interpolation and a higher-order discretization; however, there is a balance between accuracy and computational cost, depending on the need. Further optimization of the implementation can be done by cleverly reusing the fast marching step when the phase field is fixed and only the extension step is needed, e.g., in the nonlinear solve for the concentration.

In the limit of large driving forces, the evolution equation behaves like an advection equation. However, we find that there is no need for the upwind or non-oscillatory schemes, possibly due to two reasons: (i) even a small surface energy term can mitigate the stability issue of the advection equation, (ii) the fact that $p'(u)$ is used instead of ∇u eases discretization error of the gradient term.

Summary of the work

The ability to perform quantitative phase field simulations is of scientific significance and practical importance. A strategy of mapping the driving force to a constant perpendicular to the interface is proposed to eliminate the constraint due to the magnitude of the driving force. We demonstrate that the driving force extension method effectively increases the stable grid size by orders of magnitude, thus, significantly reducing the computational cost of phase field simulations. The proposed method requires a simple modification of the phase field equation and relies on well-developed algorithms; thus, it can be easily adapted with various numerical techniques. We expect this simple modification to apply directly to most phase field models. Note that if the physical problem relies on an interface width smaller than the enhanced interface width by the proposed method, like in the problem of solute trapping or particle coalescence, there is no benefit from the proposed method. In the future, we expect to extend the proposed method to more applications, e.g., handling anisotropy with an anisotropic driving force extension algorithm and extending to problems with multiple phases.

METHODS

Evolution of solid-liquid interface in additive manufacturing

We model the development of a solid-liquid interface with a moving laser source in the absolute stability limit. For demonstration purposes, we use a simplified version of the model in¹⁶. The evolution equation is given by the following Allen-Cahn equation

$$\tau \frac{\partial u}{\partial t} = \kappa \nabla^2 u - mg'(u) + p'(u) \left(L_v \frac{T_m - T}{T_m} \right), \quad (9)$$

where $\tau = 6lL_v/(\mu T_m)$, $\kappa = 6\gamma l$, $m = 3\gamma/l$, L_v is the latent heat, T and T_m are the temperature field induced by the laser and the melting temperature respectively, μ is the kinetic coefficient, and γ is the surface energy. The double-well potential is $g(u) = u^2(1-u)^2$. The third- and fifth-order interpolation functions are $p(u) = u^2(3-2u)$ and $p(u) = u^3(6u^2 - 15u + 10)$, respectively. The equation is coupled to a temperature model with the frozen temperature approximation. We use a 1D cut of the 3D Rosenthal's solution for a steady-state temperature field with a moving point source²⁷

$$T = T_0 + \frac{q}{4\pi k_T r} \exp\left(-\frac{v}{2D_T}(\xi + r)\right), \quad (10)$$

$$r = \sqrt{\xi^2 + y^2 + z^2}, \quad \xi = x - vt$$

where T_0 is the ambient temperature, q is the power of the laser, k_T is the thermal conductivity, D_T is the thermal diffusivity, x, y, z are the global/lab coordinates, v is the laser velocity, ξ is the local coordinate, and r is the distance to the center of the laser point on the sample.

The materials parameters used in this work are¹⁶: $L_v = 10^9 \text{ J m}^{-3}$, $\gamma = 0.2 \text{ J m}^{-2}$, $\mu = 1 \text{ ms}^{-1} \text{ K}^{-1}$, $T_l = 1700 \text{ K}$, $k_T = 27 \text{ W m}^{-1} \text{ K}^{-1}$, and $D_T = 5.2 \times 10^{-6} \text{ m}^2 \text{ s}^{-1}$. Processing parameters are $T_0 = 300 \text{ K}$, $q = 25 \text{ W}$, $v = 3 \text{ ms}^{-1}$. Unless otherwise mentioned, the diffuse interface width is chosen to be $l = 1.5\Delta x$ throughout this paper, where Δx is the grid size. This is equivalent to 8–10 grid points across the interface. A zero-Neumann boundary condition is used for the phase field variable. Here we choose μ large enough to make both the melting and solidifying fronts follow the temperature profile, so analytically the two interfaces move at constant velocity v . The relative error is calculated as the root-mean-square error $\text{RMS}((x_i/t_i - v)/v)$, where x_i is the interface location at time t_i . Note that both interfaces are considered when calculating the error.

Solidification: KKS model

The evolution equations in the KKS model^{4,17} are

$$\frac{1}{L} \frac{\partial u}{\partial t} = \kappa \nabla^2 u - mg'(u) - p'(u) (f^s - f^l - (c^s - c^l)\bar{\mu}), \quad (11)$$

$$\frac{\partial c}{\partial t} = \nabla \cdot (M \nabla \bar{\mu}), \quad (12)$$

where c^s and c^l are the solid and liquid concentrations, $c = p(u)c^s + (1-p(u))c^l$ is the mixture concentration, $\bar{\mu}$ is the diffusion potential, $M = p(u)M^s + (1-p(u))M^l$ is the mixture mobility. For phase α , $M^\alpha = D^\alpha \chi^\alpha$ with $\chi^\alpha = \partial c^\alpha / \partial \bar{\mu}$ the susceptibility and D^α the diffusivity. The free energy densities of the respective phases are f^s and f^l , which are chosen as a parabolic form for simplicity

$$f^a = A^a + \frac{1}{2} B^a (x^a - x_0^a)^2, \quad a = s, l, \quad (13)$$

where $x^a = V_m c^a$ is the molar fraction and V_m is the molar volume. The phase field mobility L is chosen to fulfill the local equilibrium condition

$$L_{\text{eq}} = \frac{D^l}{6a l^2 B^l (x_{\text{eq}}^l - x_{\text{eq}}^s)^2}, \quad (14)$$

where $a = 5/6$ for the third-order interpolation and $a = 47/60$ for the fifth-order interpolation, and x_{eq}^l and x_{eq}^s are the common-tangent molar fractions. Note that this expression is derived from the thin interface analysis, which requires the local equilibrium to be satisfied asymptotically; therefore, variation of the driving force within the diffuse interface still exists, due to higher-order asymptotics. This explains why there are instability issues even with local equilibrium, especially with a thick interface.

For the special case $B^s = B^l = B$ and $A^s = A^l = 0$, the driving force is

$$F = f^s - f^l - (c^s - c^l)\bar{\mu} = \frac{1}{2} B \left((x^l)^2 + (x^s)^2 - (x_0^l)^2 - (x_0^s)^2 \right). \quad (15)$$

This means we can control the magnitude of the driving force by the parameter B .

The materials parameters used in this work are²⁸: $x_0^l = 0.9$, $x_0^s = 0.1$, $A^l = A^s = 0 \text{ J m}^{-3}$, $D^s = D^l = 4.4 \times 10^{-9} \text{ m}^2 \text{ s}^{-1}$, $\gamma = 0.44216 \text{ J m}^{-2}$, and $V_m = 1.1 \times 10^{-5} \text{ m}^3 \text{ mol}^{-1}$. Note the materials parameters are chosen to make the sharp interface solution independent of B^l . For the simulations in section "Application 2: solidification", the zero-Neumann boundary condition is used for the phase field variable and the left side of the concentration. The right side of the concentration is fixed to be $x^l = 0.5$ by the Dirichlet boundary condition. The initial phase field has the equilibrium hyperbolic tangent profile and the initial concentration has a linear distribution inside the liquid. The relative error is calculated with respect to a reference simulation (fifth-order interpolation and $\Delta x = 10 \text{ nm}$): $\text{RMS}((x_i - x_i^{\text{ref}})/x_i^{\text{ref}})$, where x_i is the interface location and x_i^{ref} is the interface location of the reference simulation. For the simulations in section "Application in 2D and 3D", the zero-Neumann boundary condition is used for the phase field variable and the Dirichlet boundary condition is used for the concentration $x^l = 0.5$. The initial condition for the concentration is determined from the analytical solution at time $t = 10 \text{ ms}$ for 2D and $t = 4 \text{ ms}$ for 3D. The initial condition of the phase field is determined from the analytical radius and the equilibrium hyperbolic tangent profile. The radius is calculated from the order parameter as $(\text{Jud}A/\pi)^{1/2}$ for 2D and $(3\text{Jud}V/(4\pi))^{1/3}$ for 3D.

Solidification: Grand potential model

To show the generality of our method, we apply the proposed driving force extension method to a different equation, where

the diffuse equation has a source term, and use it to test the capillarity. The evolution equations in the grand potential model⁶ are

$$\frac{1}{L} \frac{\partial u}{\partial t} = \kappa \nabla^2 u - mg'(u) - p'(u)(\omega^s - \omega'), \quad (16)$$

$$\chi \frac{\partial \tilde{\mu}}{\partial t} = \nabla \cdot (M \nabla \tilde{\mu}) - p'(u)(c^s - c') \frac{\partial u}{\partial t}, \quad (17)$$

where ω^a is the grand potential density of phase a , $\chi = p(u)$, $\chi^s + (1 - p(u))\chi'$ is the mixture susceptibility, and the phase field mobility is given by $L = \mu T_m / (6L_v)$. The rest of the symbols have the same definitions as in previous models. For diffusion-limited growth, the local equilibrium assumption is used and the phase field mobility is replaced by

$$L_{eq} = \frac{V_m^2 D^l \chi_{eq}^l}{6a l^2 (\chi_{eq}^l - \chi_{eq}^s)^2}, \quad (18)$$

where a , χ_{eq}^l and χ_{eq}^s have the same definitions as before, and χ_{eq}^l is determined from χ_{eq}^l .

We use the dilute binary alloy free energy

$$V_m f^a = C^a + E^a x^a + RT(x^a \ln x^a - x^a), \quad a = s, l, \quad (19)$$

from which the grand potential density can be determined: $\omega^a = f^a - \tilde{\mu} c^a$ ⁶. The materials parameters are the same as in the KKS model, except $T = 880.3^\circ\text{C}$, $T_m = 933.3^\circ\text{C}$, and the free energy parameters $C^s = -37579 \text{ J mol}^{-1}$, $E^s = -20000 \text{ J mol}^{-1}$, $C^l = -36957 \text{ J mol}^{-1}$, and $E^l = -33885 \text{ J mol}^{-1}$ ²⁸.

To check the capillary effect, we solve the quasi-steady-state equation by setting $\partial \tilde{\mu} / \partial t = 0$. The liquid concentration x^l at the interface is determined from $\tilde{\mu}$ and interpolated to $u = 1/2$. Boundary and initial conditions are the same as in the KKS model.

Velocity extension algorithm

The driving force extension in Eq. (4) can be done with the velocity extension algorithm¹⁹, which solves the Eikonal equation

$$|\nabla \phi| = 1, \quad (20)$$

and the extension equation

$$\nabla F \cdot \nabla \phi = 0, \quad (21)$$

to get the signed distance to the interface ϕ and the extended driving force F . The algorithm typically involves two steps, a marching step to get ϕ and an extension step to get F . There are two types of boundary conditions for the velocity extension. The external boundary condition on the outside of the system can be the same as the phase field variable or using linear extrapolation. The internal boundary condition for the distance field is $\phi(u(\mathbf{x}) = 1/2) = 0$.

Reporting summary

Further information on research design is available in the Nature Portfolio Reporting Summary linked to this article.

DATA AVAILABILITY

The data supporting the findings of this study are available from the corresponding author upon reasonable request.

CODE AVAILABILITY

The code supporting the findings of this study are available from the corresponding author upon reasonable request.

Received: 27 April 2023; Accepted: 18 August 2023;

Published online: 08 September 2023

REFERENCES

1. Glasner, K. Nonlinear preconditioning for diffuse interfaces. *J. Comput. Phys.* **174**, 695–711 (2001).
2. Karma, A. Phase-field formulation for quantitative modeling of alloy solidification. *Phys. Rev. Lett.* **87**, 115701 (2001).
3. Echebarria, B., Folch, R., Karma, A. & Plapp, M. Quantitative phase-field model of alloy solidification. *Phys. Rev. E* **70**, 061604 (2004).
4. Kim, S. G. A phase-field model with antitrapping current for multicomponent alloys with arbitrary thermodynamic properties. *Acta Mater.* **55**, 4391–4399 (2007).
5. Moelans, N. A quantitative and thermodynamically consistent phase-field interpolation function for multi-phase systems. *Acta Mater.* **59**, 1077–1086 (2011).
6. Plapp, M. Unified derivation of phase-field models for alloy solidification from a grand-potential functional. *Phys. Rev. E* **84**, 031601 (2011).
7. Provatas, N., Pinomaa, T. & Ofori-Opoku, N. *Quantitative Phase Field Modelling of Solidification* (CRC Press, 2021).
8. Steinbach, I. et al. A phase field concept for multiphase systems. *Phys. D Nonlinear Phenom.* **94**, 135–147 (1996).
9. Nestler, B., Garcke, H. & Stinner, B. Multicomponent alloy solidification: Phase-field modeling and simulations. *Phys. Rev. E* **71**, 041609 (2005).
10. Ji, Y. & Chen, L.-Q. Phase-field model of stoichiometric compounds and solution phases. *Acta Mater.* **234**, 118007 (2022).
11. Wang, S.-L. et al. Thermodynamically-consistent phase-field models for solidification. *Phys. D Nonlinear Phenom.* **69**, 189–200 (1993).
12. Finel, A. et al. Sharp phase field method. *Phys. Rev. Lett.* **121**, 025501 (2018).
13. Fleck, M. & Schleifer, F. Sharp phase-field modeling of isotropic solidification with a super efficient spatial resolution. *Eng. Comput.* **39**, 1699–1709 (2022).
14. Feyen, V. & Moelans, N. Quantitative high driving force phase-field model for multi-grain structures. *Acta Mater.* **256**, 119087 (2023).
15. Allen, S. M. & Cahn, J. W. A microscopic theory for antiphase boundary motion and its application to antiphase domain coarsening. *Acta Metall.* **27**, 1085–1095 (1979).
16. Chadwick, A. F. & Voorhees, P. W. The development of grain structure during additive manufacturing. *Acta Mater.* **211**, 116862 (2021).
17. Kim, S. G., Kim, W. T. & Suzuki, T. Phase-field model for binary alloys. *Phys. Rev. E* **60**, 7186–7197 (1999).
18. Galenko, P. & Jou, D. Rapid solidification as non-ergodic phenomenon. *Phys. Rep.* **818**, 1–70 (2019).
19. Adalsteinsson, D. & Sethian, J. The fast construction of extension velocities in level set methods. *J. Comput. Phys.* **148**, 2–22 (1999).
20. Chopp, D. L. Another look at velocity extensions in the level set method. *SIAM J. Sci. Comput.* **31**, 3255–3273 (2009).
21. Ratke, L. & Voorhees, P. W. *Growth and coarsening: Ostwald ripening in material processing* (Springer Science & Business Media, 2002).
22. Zhao, H. A fast sweeping method for eikonal equations. *Math. Comp.* **74**, 603–627 (2004).
23. Jeong, W.-K. & Whitaker, R. T. A fast iterative method for eikonal equations. *SIAM J. Sci. Comput.* **30**, 2512–2534 (2008).
24. Hong, S., Jang, G. & Jeong, W.-K. MG-FIM: A multi-GPU fast iterative method using adaptive domain decomposition. *SIAM J. Sci. Comput.* **44**, C54–C76 (2022).
25. Kimmel, R. & Sethian, J. A. Computing geodesic paths on manifolds. *Proc. Natl. Acad. Sci.* **95**, 8431–8435 (1998).
26. Covello, P. & Rodrigue, G. Solving the eikonal equation on an adaptive mesh. *Appl. Math. Comput.* **166**, 678–695 (2005).
27. Rosenthal, D. The theory of moving sources of heat and its application to metal treatments. *Trans. ASME* **68**, 849–866 (1946).
28. Zhang, J., Poulsen, S. O., Gibbs, J. W., Voorhees, P. W. & Poulsen, H. F. Determining material parameters using phase-field simulations and experiments. *Acta Mater.* **129**, 229–238 (2017).

ACKNOWLEDGEMENTS

This work is sponsored by the Office of Naval Research (ONR) under grant N00014-20-1-2327. Additional support is provided in part through the computational resources and staff contributions provided for the Quest high performance computing facility at Northwestern University which is jointly supported by the Office of the Provost, the Office for Research, and Northwestern University Information Technology.

AUTHOR CONTRIBUTIONS

J.Z. conceived the idea under the supervision of P.V.. A.C. contributed to the discussion and the design of test cases. D.C. wrote the velocity extension code. J.Z. wrote the initial draft. All authors contributed to the writing of the manuscript and approved the final manuscript.

COMPETING INTERESTS

The authors declare no competing interests.

ADDITIONAL INFORMATION

Supplementary information The online version contains supplementary material available at <https://doi.org/10.1038/s41524-023-01118-0>.

Correspondence and requests for materials should be addressed to Jin Zhang.

Reprints and permission information is available at <http://www.nature.com/reprints>

Publisher's note Springer Nature remains neutral with regard to jurisdictional claims in published maps and institutional affiliations.



Open Access This article is licensed under a Creative Commons Attribution 4.0 International License, which permits use, sharing, adaptation, distribution and reproduction in any medium or format, as long as you give appropriate credit to the original author(s) and the source, provide a link to the Creative Commons license, and indicate if changes were made. The images or other third party material in this article are included in the article's Creative Commons license, unless indicated otherwise in a credit line to the material. If material is not included in the article's Creative Commons license and your intended use is not permitted by statutory regulation or exceeds the permitted use, you will need to obtain permission directly from the copyright holder. To view a copy of this license, visit <http://creativecommons.org/licenses/by/4.0/>.

© The Author(s) 2023